Atomistic modeling of femtosecond laser-induced melting and atomic mixing in Au film – Cu substrate system

Derek A. Thomas [a], Zhibin Lin [a], Leonid V. Zhigilei [a,*], Evgeny L. Gurevich [b], Silke Kittel [b], Roland Hergenröder [b]

[a] Department of Materials Science and Engineering, University of Virginia, 395 McCormick Road, Charlottesville, VA 22904-4745, United States
[b] ISAS - Institute for Analytical Sciences, Department of Material Analysis Bunsen-Kirchhoff-Str. 11, 44139 Dortmund, Germany

ABSTRACT

The mechanisms of femtosecond laser-induced transient melting and atomic mixing in a target composed of a 30 nm Au film deposited on a bulk Cu substrate are investigated in a series of atomistic simulations. The relative strength and the electron temperature dependence of the electron–phonon coupling of the metals composing the layered target are identified as major factors affecting the initial energy redistribution and the location of the region(s) undergoing transient melting and resolidification. The higher strength of the electron–phonon coupling in Cu, as compared to Au, results in a preferential sub-surface heating and melting of the Cu substrate, while the overlaying Au film largely retains its original crystalline structure. The large difference in the atomic mobility in the transiently melted and crystalline regions of the target makes it possible to connect the final distributions of the components in the resolidified targets to the history of the laser-induced melting process, thus allowing for experimental verification of the computational predictions.

© 2009 Elsevier B.V. All rights reserved.

1. Introduction

Surface modification by laser irradiation is in the core of many modern processing and fabrication techniques, including laser surface alloying, cladding, annealing, and hardening, e.g. [1–6]. The improvement of surface properties is achieved by structural and compositional surface modification through the formation of metastable crystalline and amorphous phases, grain refinement, generation/annealing of crystal defects, redistribution of the alloying elements, and changes in the phase segregation patterns. While it is highly desirable to be able to predict the final concentration profiles and phase composition in laser-treated targets, there have been limited experimental and computational studies directed specifically at investigation of compositional changes and microstructure development in short (picosecond and femtosecond) pulse laser processing.

Most of the methods of laser surface modification involve melting and subsequent resolidification of a surface region. Melts have high atomic mobility and usually unlimited solubility, enabling a rapid mixing and homogenization of the alloy.

Experimental analysis of the laser-treated surface layer can provide information on the microstructure and phases generated in the course of rapid solidification, which, in turn, may be related to the kinetics and mechanisms of the partitioning of the alloy components at the liquid–crystal interfaces, velocity of the epitaxial re-growth of the substrate, as well as nucleation and growth of new phases. Indeed, for continuous laser treatment, a detailed and systematic analysis of sections of the laser traces has been performed and resulted in Solidification Microstructure Processing Maps developed for a number of binary and ternary systems, e.g. [7–9]. In this case, the laser-affected zones are large (on the order of mm) and microstructures can be easily studied by optical or transmission electron microscopy.

In the case of short (picosecond or femtosecond) pulse laser irradiation, however, the surface layer subjected to laser melting and resolidification can be as small as tens of nanometers, making characterization of laser-induced microstructural changes challenging [10–13]. At the same time, the small size of the laser-modified zone and the short time of the melting–resolidification cycle (from hundreds of picoseconds to tens of nanoseconds at fluences below the permanent damage threshold, as deduced from pump-probe experimental measurements [14–16]) suggest a possibility for direct atomic-level modeling of processes involved in short pulse laser processing. Computa-

tional modeling can provide information on the fundamental processes responsible for the laser-induced surface modification and may help in physical interpretation of the results of experimental probing of the laser-modified zone.

As a first step in the investigation of the mechanisms and kinetics of atomic mixing and structural transformations in multi-component targets irradiated by short laser pulses, we perform a series of atomistic simulations of femtosecond laser processing of thin Au films deposited on a Cu substrate. The computational model designed for atomistic simulations of laser interactions with the layered target is described next, in Section 2. The results of the simulations are presented and discussed in Section 3 and summarised in Section 4.

2. Computational model

The mechanisms of atomic mixing and associated compositional changes in the target composed of a bulk Cu substrate and a 30 nm Au layer are investigated with a combined atomistic-continuum model [17], where the classical molecular dynamic (MD) method is incorporated into the general framework of the two-temperature model (TTM) [18] describing the time evolution of the lattice and electron temperatures by two coupled nonlinear differential equations. A complete description of the TTM-MD model is given elsewhere [17]. Below we provide the details of the computational setup designed for the simulation of the laser interaction with the layered Cu–Au target.

Interatomic interactions in the MD part of the model are described by the embedded-atom method (EAM) potential in the form suggested by Foiles, Baskes, and Daw (FBD) [19]. This potential provides a relatively good description of thermodynamic properties of Au and Cu, as well as their binary alloy. The parameters of the FBD EAM potential for the Au-Cu cross-interaction are fitted to the heat of mixing for dilute solutions. The original FBD parameterization does not specify a cutoff distance for interatomic interactions and, to improve the computational efficiency of the potential, a cutoff function suggested in Ref. [20] is used in this work to smoothly bring the interaction energies and forces to zero at a cutoff distance of 5.5 Å. To test the implementation of the potential, the equilibrium melting temperatures of pure Au and Cu are calculated in a series of liquid–crystal coexistence simulations. The values of 1063 K for Au and 1290 K for Cu match closely the result of earlier calculations for FBD EAM Cu [21] and are in a reasonable agreement with experimental values of 1336 K for Au and 1356 K for Cu [22].

A schematic sketch of the computational system used in the simulation is shown in Fig. 1. The atomic-level representation is used for the 30 nm Au film and a top 200 nm region of the Cu substrate, whereas the rest of the target is represented at the continuum level, with the conventional TTM. The size of the continuum region is chosen to be 1770 nm, so that no significant changes in the electron and lattice temperatures are observed at the bottom of the computational system during the time of the simulations. The atomic part of the model is composed of 178,200 Cu and 18,688 Au atoms initially arranged in fcc crystallites with lateral dimensions of 3.27 nm × 3.27 nm and periodic boundary conditions imposed in the directions parallel to the surface of the target. The film and the substrate have the same crystallographic orientation, with (1 0 0) planes oriented parallel to the surface of the target. The lateral size of the computational system corresponds to nine fcc unit cells in each direction for the Cu substrate and eight slightly compressed fcc unit cells for the Au film. This size is chosen to minimize the lateral strain in the film introduced by matching the lateral size of the substrate (the strain is 0.46% for the Au film at 300 K). The next minimum of the strain corresponds to a twice-larger lateral size, bringing the number of atoms in the system close to 800,000 and significantly
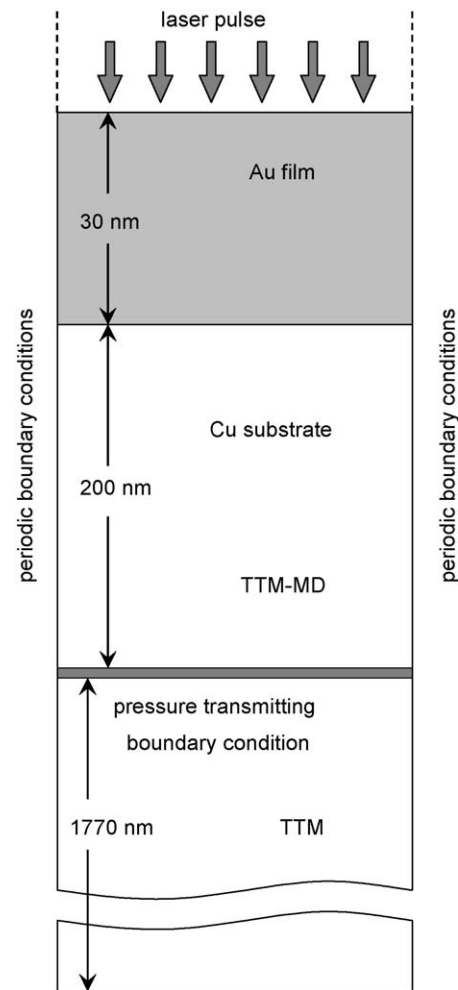
Fig. 1. Schematic sketch of the simulation setup. The 30 nm Au film and a 200 nm part of the Cu substrate are represented with atomic-level resolution, using the TTM-MD model, whereas the electron heat conduction in the deeper part of the substrate is simulated with the conventional TTM.

increasing the computational cost of the simulations. Before applying laser irradiation, the initial system is equilibrated in an MD simulation performed for 100 ps at 300 K. This time is found to be sufficient for complete dissipation of the pressure wave induced by the initial expansion of the laterally compressed film in the direction normal to the surface.

At the bottom of the MD part of the model, a pressure-transmitting, heat-conducting boundary condition is used to account for the energy transfer from the surface region of the target, represented with atomic-level resolution, to the deeper part of the target, represented at the continuum level. The combined TTM-MD model, briefly discussed above, provides a natural description of the electron heat conduction from the atomistic to the continuum regions. In order to avoid an artificial reflection of the laser-induced pressure wave propagating from the irradiated surface region to the bulk of the target, a special pressure-transmitting boundary condition [23,24] is applied at the bottom of the MD part of the model. The energy carried away by the pressure wave though the pressure-transmitting boundary condition can be monitored, allowing for control over the energy conservation in the combined model [25]. An illustration of the non-reflective propagation of the pressure wave from the atomistic to the continuum parts of the model, as well as the seamless transition in the temperature fields between the two parts of the model, can be seen in Figs. 2 and 5.
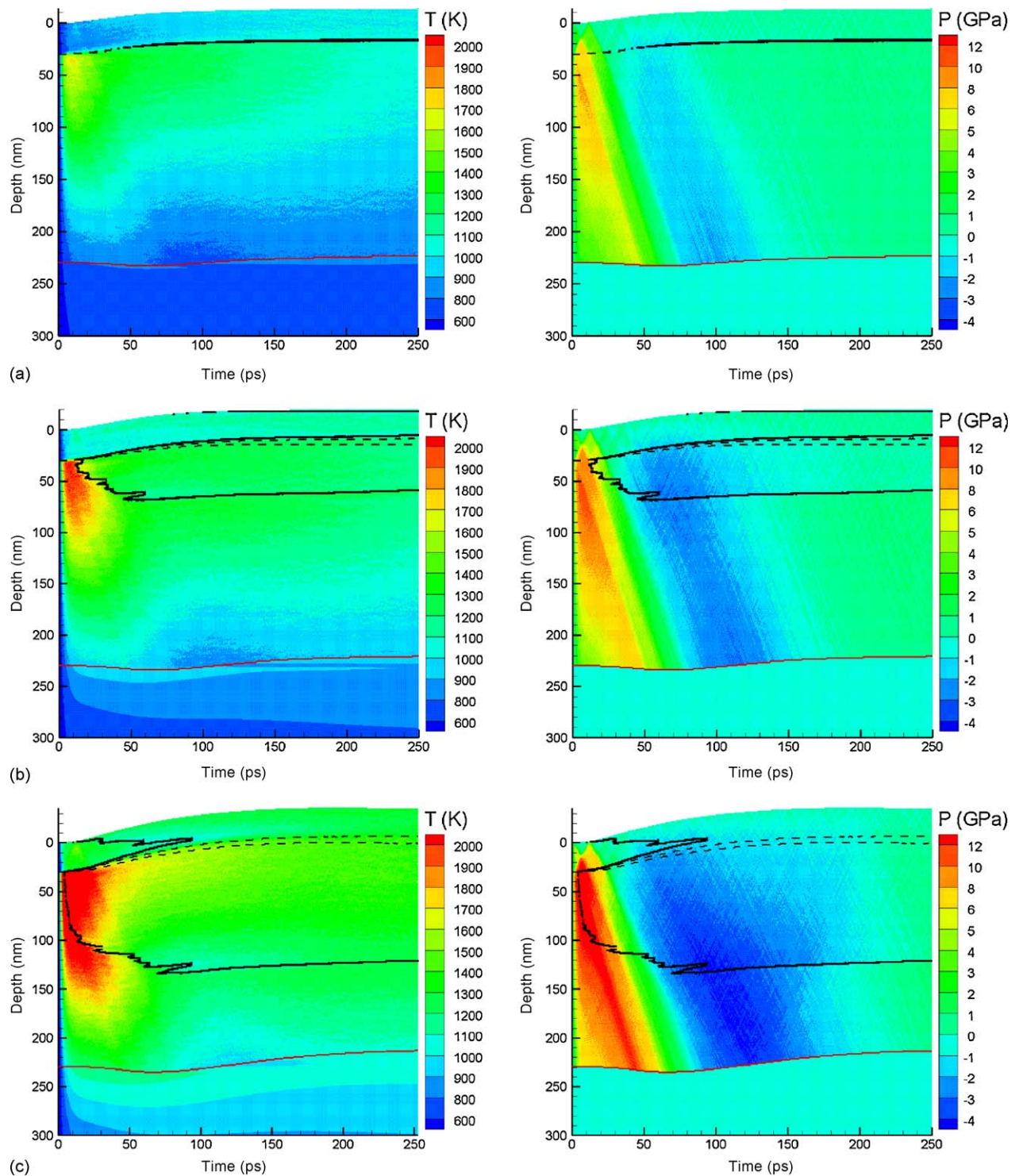
Fig. 2. Contour plots of the lattice temperature and pressure for simulations of a Cu–Au target (see Fig. 1) irradiated with 200 fs laser pulses at absorbed fluences of (a) 100 mJ/cm², (b) 130 mJ/cm², and (c) 180 mJ/cm². The ballistic energy transport is accounted for by assuming an effective range of the laser energy deposition of $\lambda_{opt} + \lambda_{ball}$ = 100 nm. Laser pulse is directed along the Y-axis, from the top of the contour plots. The black lines separate the melted regions from the crystalline bulk of the target. Black dashed lines outline the regions of atomic mixing defined as the regions were at least 1 at.% of the second component is present. Red lines separate the MD and continuum parts of the combined TTM-MD model.

The electron temperature dependences of the thermophysical material properties included in the TTM equation for the electron temperature (the electron–phonon coupling factor, the electron heat capacity, and the thermal conductivity) are taken in the forms that account for the contribution from the thermal excitation from the electron states below the Fermi level [26,27]. The large positive deviations of the electron heat capacity from the linear dependence and the sharp increases in the strength of the electron–phonon coupling, predicted for Au and Cu at electron temperatures exceeding ~3000 K, can have a significant effect of the initial energy redistribution and the depth of the region undergoing transient melting and resolidification in the Cu–Au target considered in this work.

The temperature dependence of the electron thermal conductivity is approximated by the Drude model relationship, $K_e(T_e, T_l) = v^2 C_e(T_e)\tau_e(T_e, T_l)/3$, where $C_e(T_e)$ is the electron heat capacity, v^2 is the mean square velocity of the electrons contributing to the electron heat conductivity, approximated in this work as the Fermi velocity squared, v_F^2, and $\tau_e(T_e, T_l)$ is the total electron scattering time defined by the electron–electron scattering rate, $1/\tau_{e-e} = AT_e^2$, and the electron–phonon scattering rate, $1/\tau_{e-ph} = BT_l$, so that $1/\tau_e = 1/\tau_{e-e} + 1/\tau_{e-ph} = AT_e^2 + BT_l$. For Au, the values of coefficients A and B are given in Refs. [17,28]. For Cu, the value of the coefficient A (2.66×10^6 s^{-1} K^{-2}) is estimated within the free electron model, following an approach suggested in Ref. [29], whereas the coefficient B (2.41×10^{11} s^{-1} K^{-1}) is obtained from the experimental value of the thermal conductivity of solid Cu at the melting temperature, 330 Wm^{-1} K^{-1} [30]. The contribution of d band electrons to the conductivity is partially accounted for by using the electron temperature dependence of the electron heat capacity, $C_e(T_e)$, given in Ref. [26], in the Drude model equation. In the region adjacent to the Cu–Au interface, the material properties included in the TTM equation for the electron temperature are calculated as linear combinations of the properties of individual components taken with weights equal to the local atomic concentrations.

Irradiation by a 200 fs laser pulse is represented through a source term with a Gaussian temporal profile and an exponential attenuation of laser intensity with depth under the surface (Beer–Lambert law) added to the TTM equation for the electron temperature. The room temperature electron mean free paths in both Au and Cu are exceeding the optical penetration depth and the thermalization of the excited electrons is likely to take place in wider surface regions of the irradiated targets. Indeed, the ballistic energy transport occurring before the thermalization of the electron gas has been found to play an important role in the initial energy redistribution in targets irradiated by femtosecond laser pulses [31–33]. In this work, the increase in the effective depth of the initial laser energy deposition due to the ballistic energy transport by nonthermal electrons is accounted for through modification of the optical absorption depth in the source term of the TTM equation [17,31]. Namely, the optical absorption depth, λ_{opt}, is substituted in the source term by an effective range of the laser energy deposition, $\lambda_{opt} + \lambda_{ball}$. The strong excitation energy dependence of the electron–electron scattering [32] does not allow for a simple estimation of the effective depth of the ballistic energy transport, with further uncertainty introduced by the modification of the scattering rates in the substrate–film interfacial region. In particular, the results of recent time-resolved optical probe measurements of the melting dynamics in a silver target irradiated by a femtosecond laser pulse [34] suggest that the heat conduction can be strongly suppressed during the initial state of strong electron–phonon nonequilibrium generated by the laser irradiation. Thus, in this work we perform simulations for two values of the effective range of the laser energy deposition ($\lambda_{opt} + \lambda_{ball}$) that we consider to be the upper and lower bound estimates of the real value, 30 and 100 nm. The comparison of the results allows us to discuss the effect of the assumption of the ballistic energy transport on the characteristics of the laser melting/resolidification process.

3. Results and discussion

The results of a series of simulations performed for the Cu–Au system at laser fluences below the threshold for material removal (ablation) are illustrated by temperature and pressure contour plots shown in Fig. 2 for three representative simulations. In all simulations, the fast energy transfer from the hot electrons excited by the laser pulse to the lattice leads to the temperature increase in the region of the target affected by the electronic heating. Although
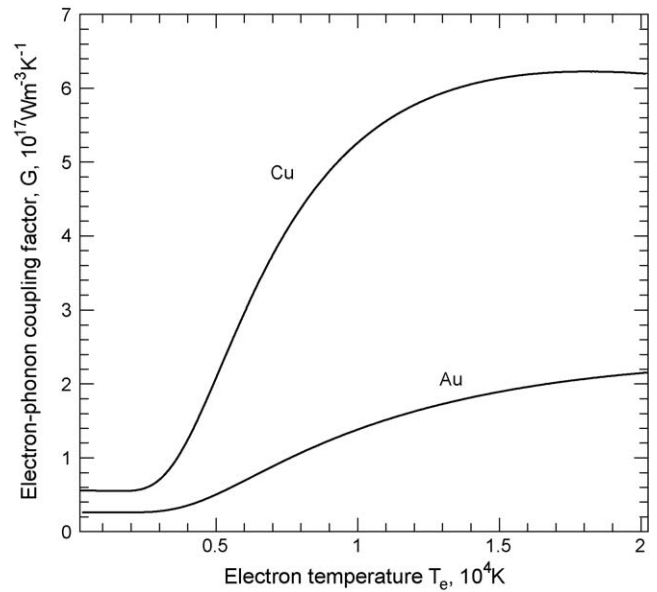
Fig. 3. The electron temperature dependence of the electron–phonon coupling factor of Cu and Au [26,27].

the electronic temperature is initially higher in the Au film, the increase of the lattice temperature is much more pronounced in the Cu substrate, where the temperature rises sharply during the first 10 ps. This preferential sub-surface heating can be explained by the difference in the strength of the electron–phonon coupling of the two materials, Fig. 3. The room temperature value of the electron–phonon coupling factor in Cu ($\sim 5.5 \times 10^{16}$ Wm^{-3} K^{-1}) is more than twice higher than the one in Au ($\sim 2.6 \times 10^{16}$ Wm^{-3} K^{-1}) [26], as predicted based on room temperature pump-probe reflectivity measurements reported in Ref. [35]. Moreover, although the two metals have similar electron densities of states, with d bands located at approximately the same depth under the Fermi level, the smaller width of the d band and a higher density of states at the high-energy edge of the d band in Cu, as compared to Au, result in a much steeper increase of the electron–phonon coupling in Cu at electron temperatures exceeding ~ 3000 K [26,27]. In particular, at an electron temperature of 10,000 K, the thermal excitation of d band electrons leads to the increase of the electron–phonon coupling factors with respect to the room temperature values by factors of 9.5 and 5.8 for Cu and Au, respectively. A similar effect of preferential sub-surface heating has also been predicted in TTM calculations performed for femtosecond laser heating of Au-Cr multi-layer targets [36]. Similarly to the Au-Cu system discussed above, the faster increase of the lattice temperature in the Cr layer is attributed to the stronger electron-phonon coupling in Cr as compared to Au.

The temperature increase in the Cu substrate occurs faster than the time needed for the mechanical relaxation (expansion) of the heated part of substrate, leading to the conditions of the inertial stress confinement [37] and resulting in the build up of high compressive thermoelastic stresses within the top ~ 100 nm region of the Cu substrate. The compressive stresses increase during the time of the lattice heating and reach maximum values of 9, 12, and 18 GPa at absorbed fluences of 100, 130, and 180 mJ/cm^2. The stresses relax by driving compressive stress waves deeper into the bulk of the target and in the direction of the free surface, Fig. 2. The stress wave propagating through the colder Au film reflects from the free surface and transforms into a tensile (unloading) wave that follows the compressive wave propagating into the bulk of the Cu substrate. The pressure-transmitting heat-conductive boundary condition, applied at the depth of 230 nm, ensures that both the compressive and tensile components of the pressure wave propagate

without any noticeable reflection from the boundary separating the TTM-MD and TTM parts of the model. The fact that the maximum pressure is generated in the Cu substrate and the generation of the unloading wave is delayed by the propagation of the compressive wave to and from the free surface through the Au film, results in a more gradual, as compared to one-component targets [37–40], transition from the compressive to the tensile components of the stress wave and a reduced amplitude of the tensile component.

The fast evolution of the laser-induced stresses plays an important role in defining the characteristics of the melting process. Although at the lowest fluence of 100 mJ/cm^2 (Fig. 2a) the lattice temperature in the upper ∼50 nm part of the Cu substrate temporarily exceeds the equilibrium melting temperature of the EAM Cu material (1290 K at zero pressure) by more than 25%, no homogeneous nucleation of the liquid phase is observed within the overheated substrate. The enhanced crystal stability against melting can be explained by the strong compressive stresses that are present in the region of the thermal spike during the first 20 ps after the laser pulse. Indeed, using zero pressure values of the volume change and entropy of melting determined for the EAM Cu material, $\Delta V_\mathrm{m} = 0.347$ cm^3/mol and $\Delta S_\mathrm{m} = \Delta H_\mathrm{m}/T_\mathrm{m} = 8.27$ J/(K mol), the pressure dependence of the melting temperature, predicted with the Clapeyron equation, is $(dT/dP)_\mathrm{m} \approx \Delta V_\mathrm{m}/\Delta S_\mathrm{m} = 42$ K/GPa. Thus, the compressive stresses of ∼6 GPa existing in the top region of the Cu substrate during the first ∼20 ps, Fig. 2a, can be expected to cause a transient increase in the melting temperature by as much as 250 K, explaining the absence of the homogeneous melting in this simulation. The combined effect of the fast electronic heat conduction from the top part of the Cu substrate and the cooling due to the adiabatic/isentropic expansion associated with the arrival of the unloading wave [17,37] results in a fast temperature drop in the top part of the Cu substrate down to below the equilibrium melting temperature by the time of 50 ps. The melting in the simulation performed at 100 mJ/cm^2 is limited to a thin region adjacent to the Cu–Au interface, mostly at the Au side. The interfacial melting starts at ∼45 ps, with melted region slowly expanding up to a width of ∼3 nm by 200 ps, and shrinking at later time.

At a higher fluence of 130 mJ/cm^2, the fast homogeneous melting of a large, ∼50 nm, part of the Cu substrate is observed during the first 50 ps of the simulation, Fig. 2b. The melting starts as early as 10 ps by the homogeneous nucleation of several liquid regions inside the overheated top part of the Cu substrate. The nucleation of the liquid regions deeper into the target continues at later times and is assisted by the tensile stresses associated with the unloading wave propagating through the melting region. A partial melting of the Au film also takes place through slow propagation of two melting fronts, from the Cu–Au interface and from the free surface of the target. By the time of 250 ps, ∼3 and ∼7 nm parts of the Au film are melted from the sides of the free surface and the interface, respectively.

At the highest fluence of 180 mJ/cm^2, the melting of the Cu substrate proceeds by the fast homogeneous melting of a strongly overheated ∼60 nm top part of the substrate during the first 10 ps after the laser pulse, followed by a slower melting of a similar part of the substrate during the next 90 ps, Fig. 2c. Similarly to the simulation performed at 130 mJ/cm^2, the second slower stage of the melting process at 180 mJ/cm^2 is assisted by the tensile stresses, exceeding −2 GPa at the time of the last instance of the homogeneous nucleation of a liquid region at a depth of ∼135 nm, as well as by the anisotropic lattice distortions associated with an uniaxial expansion of the crystalline part of the target in the direction normal to the surface [41]. Despite the slower rate of the electron–phonon energy transfer in the Au film, the maximum overheating in the film exceeds 20% above the equilibrium melting temperature of the EAM Au material (1063 K at zero pressure) by the time of ∼12 ps after the laser pulse. The strong overheating results in the complete melting of the film by the time of ∼90 ps.

The characteristics of the melting process and the temperature evolution in the Cu–Au system have direct implications on the kinetics of atomic mixing and the final concentration profiles that are produced by the laser processing of the layered target. Although the time of the simulations reported in this work is too short to observe the complete solidification even for the lowest laser fluence of 100 mJ/cm^2, the concentration profiles shown in Fig. 4 for the time of 250 ps after the laser pulse do provide some preliminary hints on the
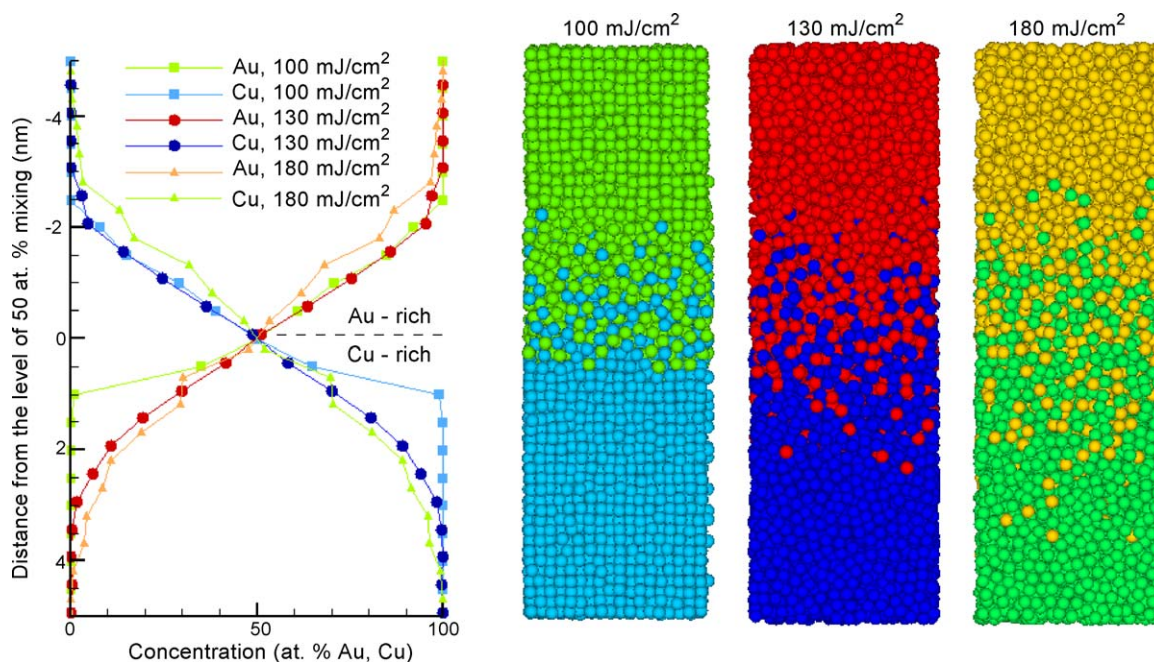
Fig. 4. Snapshots of atomic configurations and concentration profiles shown for the region of the Cu–Au interface at a time of 250 ps in simulations performed with $\lambda_\mathrm{opt} + \lambda_\mathrm{ball} = 100$ nm at absorbed fluence of 100, 130, and 180 mJ/cm^2 (see Fig. 2). The colors used for Cu and Au atoms in the snapshots match the corresponding colors of the concentration profiles.

characteristic features of the final concentration profiles that can be expected in the targets after the resolidification. In particular, the concentration profiles observed at the lowest fluence of 100 mJ/cm^2 exhibit a pronounced asymmetry, with Cu atoms diffusing further into the Au film as compared to Au diffusion into the Cu substrate. This asymmetry of the concentration profiles can be related to the asymmetry in the interfacial melting that proceeds mainly on the

side of Au, which has a lower melting temperature. Interestingly, the effect of the asymmetric diffusion disappears and may even reverse its direction at a higher fluence of 130 mJ/cm^2, when a weak trend of preferential diffusion of Au into Cu can be identified and related to the more extensive melting of the Cu substrate as compared to the Au film. This asymmetry is likely to become more pronounced with time, as the crystalline part of the Au film is located relatively close to
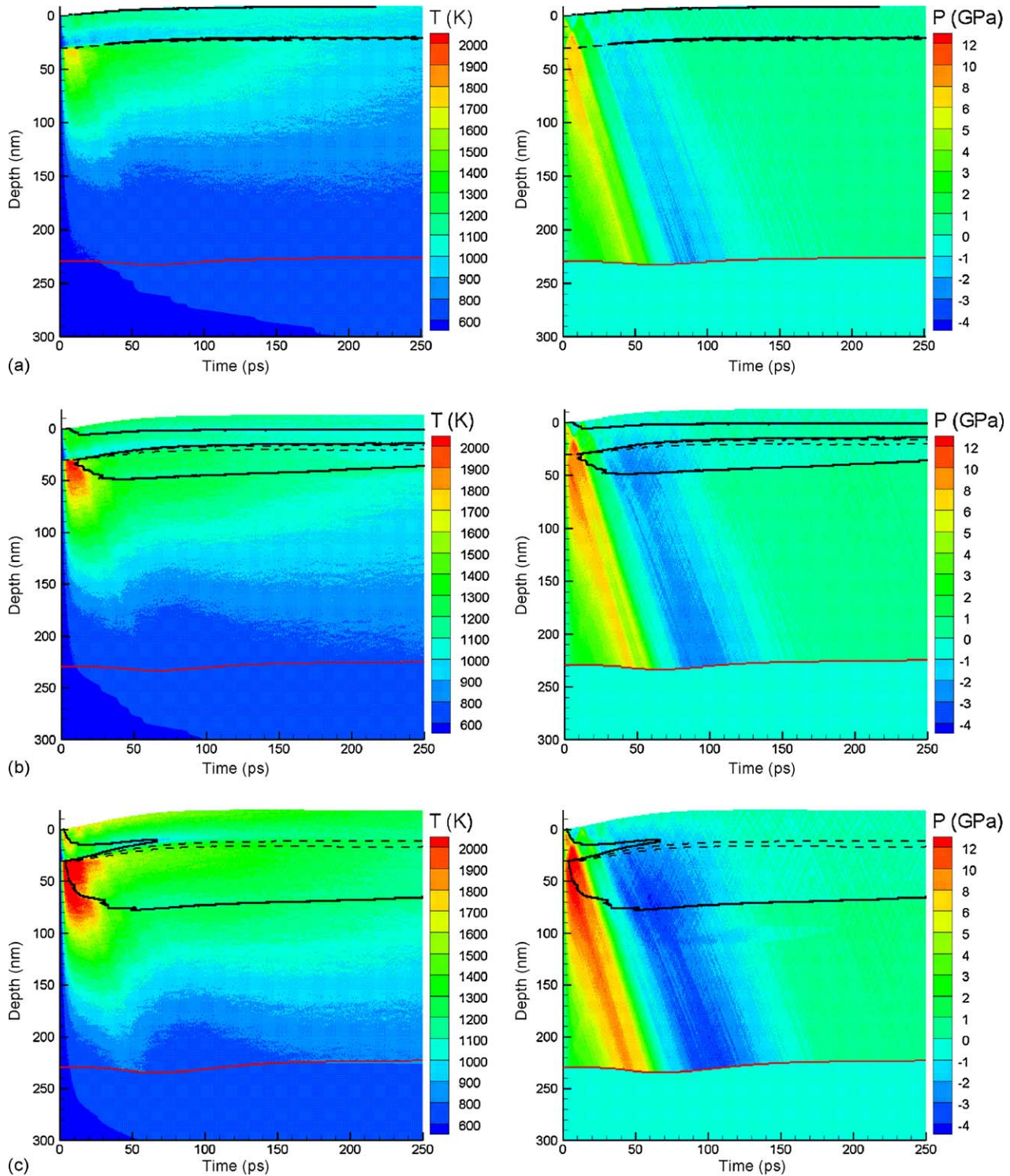
Fig. 5. Contour plots of the lattice temperature and pressure for simulations of a Cu–Au target irradiated with 200 fs laser pulses at absorbed fluences of (a) 80 mJ/cm^2, (b) 100 mJ/cm^2, and (c) 130 mJ/cm^2. The simulations are performed under conditions similar to the ones used in the simulations illustrated in Fig. 2, but with shorter effective range of the laser energy deposition, $\lambda_{opt} + \lambda_{ball} = 30$ nm. Laser pulse is directed along the Y-axis, from the top of the contour plots. The black lines separate the melted regions from the crystalline bulk of the target. Black dashed lines outline the regions of atomic mixing defined as the regions were at least 1 at.% of the second component is present. Red lines separate the MD and continuum parts of the combined TTM-MD model.

the interfacial region and would provide a natural limit for the active diffusion of Cu atoms into the film.

At the highest fluence of 180 mJ/cm^2, the complete melting of the film and the longer time of resolidification provide the conditions for a thorough mixing of the Cu and Au atoms in the surface region of the target. Combined with the high cooling rate, the mixing may result in the formation of a thin amorphous layer in the surface region of the target. This hypothesis is currently investigated in several long-time scale simulations.

As briefly discussed in Section 2, the presence of the substrate–film interface, along with the strong energy dependence of the electron–electron scattering, introduce an uncertainty into the estimation of the effective depth of the ballistic energy transport. In the simulations discussed above, the value of the effective range of the laser energy deposition, $\lambda_{opt} + \lambda_{ball}$, is assumed to be 100 nm. In order to evaluate the sensitivity of the results of the simulations to this assumption, a series of simulations is also performed for much smaller value of the effective range of the laser energy deposition, $\lambda_{opt} + \lambda_{ball}$ = 30 nm. The results of the simulations are illustrated by the temperature and pressure contour plots shown for absorbed fluences of 80, 100, and 130 mJ/cm^2 in Fig. 5. Qualitatively, the results are similar to the ones obtained with the assumption of a larger range of ballistic electrons. The lattice temperature increase is still much faster in the Cu substrate than in the Au film, leading to the preferential sub-surface melting of the substrate. The shorter range of the laser energy deposition, however, results in the localization of the lattice heating within a smaller surface region of the target. The faster and more localized lattice heating is facilitated by the substantial increase in the strength of the electron–phonon coupling with increasing electron temperature, predicted for both Au and Cu, Fig. 3. As a result, the processes comparable to the ones observed in the simulations performed with the larger range of the ballistic energy transport, Fig. 2, are taking place at substantially lower fluences. In particular, an interfacial melting limited to a thin Au region adjacent to the Cu–Au interface takes place at a fluence of 80 mJ/cm^2 (Fig. 5a), a sub-surface melting of the Cu substrate and a significant surface melting of the Au film is observed at a fluence of 100 mJ/cm^2 (Fig. 5b), and a complete melting of the film is observed at a fluence of 130 mJ/cm^2 (Fig. 5c). The similarity in the characteristics of the melting process between the simulations performed with the two different values of the range of the ballistic energy transport are reflected in the similar fluence dependences of the concentration profiles in the irradiated target, with asymmetric concentration profile defined by the Cu diffusion into a transiently melted Au layer adjacent to the Cu–Au interface observed at 80 mJ/cm^2 (similar to the profile shown in Fig. 4 for 100 mJ/cm^2) and almost symmetric interdiffusion at higher fluences (similar to the profiles shown in Fig. 4 for 130 and 180 mJ/cm^2).

The initial experiments performed for Cu–Au system, albeit for a different configuration (200 nm Au and 50 nm Cu layers deposited subsequently on a glass substrate and irradiated through the glass by a 200 fs laser pulse), have demonstrated the ability to generate and detect the interfacial mixing. In particular, the concentration profiles measured for the laser-processes areas in the target with a combination of sputtering and X-ray photoelectron spectroscopy are found to exhibit an asymmetric interdiffusion (preferential diffusion of Cu into Au), and a non-monotonous dependence of the atomic mixing on the laser fluence. Further simulations and experiments are being designed for systems that would allow for the direct quantitative comparison between the experimental measurements and computational predictions.

4. Summary

The results of the atomistic simulations of femtosecond laser processing of a Au film–Cu substrate system suggest that the relative strength and the electron temperature dependence of the electron–phonon coupling of the materials composing the layered target are playing an important role in defining both the characteristics of the melting process and the concentration profiles in the surface region of the irradiated target. The higher strength of the electron–phonon coupling in Cu, as compared to Au, results in the redistribution of the deposited laser energy from the Au film to the Cu substrate, where the energy of the excited electrons couples more effectively to the lattice vibrations, leading to the preferential lattice heating in the substrate. At laser fluences close to the melting threshold, the preferential lattice heating results in the selective sub-surface melting of the Cu substrate, whereas the overlaying Au film largely retains its original crystalline structure, even though EAM Au has a substantially lower melting temperature than EAM Cu (1063 K for EAM Au vs. 1290 K for EAM Cu). Note that the smaller difference in the experimental melting temperatures of Au and Cu (1336 K for Au vs. 1356 K for Cu) suggests that the effect of the selective sub-surface melting of the Cu substrate, predicted in the simulations, should be even more pronounced in experiments.

The unusual melting behavior of the layered target has direct implications on the kinetics of atomic mixing. The large difference in the atomic mobility in the transiently melted and crystalline regions of the target makes it possible to connect the final distributions of the components in the resolidified targets to the history of the laser-induced melting process, thus allowing for experimental verification of the computational predictions. Although significantly longer (nanoseconds) simulations are needed to achieve the complete solidification of the melted parts of the target, the preliminary results reported in this paper illustrate the direct connections between the characteristics of the melting process and the evolution of the concentration profiles, suggesting an interesting direction for further computational and experimental exploration.

References

[1] D. Bäuerle, Laser Processing and Chemistry, Springer-Verlag, Berlin, Heidelberg, 2000.
[2] P.A. Molian, in: T.S. Sudarshan (Ed.), Surface Modification Technologies, Marcel-Dekker, New York, 1989, pp. 421–492.
[3] C.J. Lin, F. Spaepen, Acta Metall. 34 (1986) 1367–1375.
[4] J.G. Hoekstra, S.B. Quadri, J.R. Scully, J.M. Fitz-Gerald, Adv. Eng. Mater. 7 (2005) 805–809.
[5] K. Biswas, K. Chattopadhyay, Metall. Mater. Trans. A 38 (2007) 1395–1406.
[6] S. Yang, Z.J. Wang, H. Kokawa, Y.S. Sato, J. Mater. Sci. 42 (2007) 847–853.
[7] W. Kurtz, Adv. Eng. Mater. 3 (2001) 443–452.
[8] O. Hunziker, W. Kurz, Acta Mater. 45 (1997) 4981–4992.
[9] Q.Y. Pan, X. Lin, W.D. Huang, Y.H. Zhou, G.L. Zhang, Mater. Res. Bull. 33 (1998) 1621–1633.
[10] V. Margetic, K. Niemax, R. Hergenröder, Anal. Chem. 75 (2003) 3435–3439.
[11] Q. Feng, Y.N. Picard, H. Liu, S.M. Yalisove, G. Mourou, T.M. Pollock, Scripta Mater. 53 (2005) 511–516.
[12] Y.N. Picard, D.P. Adams, S.M. Yalisove, Mater. Res. Soc. Symp. Proc. 850 (2005) MM1.9.
[13] R. Le Harzic, N. Huot, E. Audouard, C. Jonin, P. Laporte, S. Valette, A. Fraczkiewicz, R. Fortunier, Appl. Phys. Lett. 80 (2002) 3886–3888.
[14] C.A. MacDonald, A.M. Malvezzi, F. Spaepen, J. Appl. Phys. 65 (1989) 129–136.
[15] M.B. Agranat, S.I. Ashitkov, V.E. Fortov, A.V. Kirillin, A.V. Kostanovskii, S.I. Anisimov, P.S. Kondratenko, Appl. Phys. A: Mater. Sci. Process 69 (1999) 637–640.
[16] M. Harbst, T.N. Hansen, C. Caleman, W.K. Fullagar, P. Jönsson, P. Sondhauss, O. Synnergren, J. Larsson, Appl. Phys. A: Mater. Sci. Process 81 (2005) 893–900.
[17] D.S. Ivanov, L.V. Zhigilei, Phys. Rev. B 68 (2003) 064114.
[18] S.I. Anisimov, B.L. Kapeliovich, T.L. Perel'man, Sov. Phys. JETP 39 (1974) 375–377.
[19] S.M. Foiles, M.I. Baskes, M.S. Daw, Phys. Rev. B 33 (1986) 7983–7991.
[20] A.F. Voter, S.P. Chen, Mater. Res. Soc. Symp. Proc. 82 (1999) 175–180.
[21] E.B. Webb III, G.S. Grest, D.R. Heine, J.J. Hoyt, Acta Mater. 53 (2005) 3163–3177.

[22] Handbook of Chemistry and Physics, 64th ed., CRC Press, Boca Raton, 1983.
[23] L.V. Zhigilei, B.J. Garrison, Mater. Res. Soc. Symp. Proc. 538 (1999) 491–496.
[24] C. Schafer, H.M. Urbassek, L.V. Zhigilei, B.J. Garrison, Comp. Mater. Sci. 24 (2002) 421–429.
[25] L.V. Zhigilei, D.S. Ivanov, Appl. Surf. Sci. 248 (2005) 433–439.
[26] Z. Lin, L.V. Zhigilei, V. Celli, Phys. Rev. B 77 (2008) 075133.
[27] http://www.faculty.virginia.edu/CompMat/electron-phonon-coupling/.
[28] X.Y. Wang, D.M. Riffe, Y.S. Lee, M.C. Downer, Phys. Rev. B 50 (1994) 8016–8019.
[29] R.H.M. Groeneveld, R. Sprik, A. Lagendijk, Phys. Rev. B 51 (1995) 11433–11445.
[30] K.C. Mills, B.J. Monaghan, B.J. Keene, Int. Mater. Rev. 41 (1996) 209–242.
[31] J. Hohlfeld, S.-S. Wellershoff, J. Güdde, U. Conrad, V. Jähnke, E. Matthias, Chem. Phys. 251 (2000) 237–258.
[32] C. Suárez, W.E. Bron, T. Juhasz, Phys. Rev. Lett. 75 (1995) 4536–4539.
[33] X. Liu, R. Stock, W. Rudolph, Phys. Rev. B 72 (2005) 195431.
[34] W.-L. Chan, R.S. Averback, D.G. Cahill, A. Lagoutchev, Phys. Rev. B 78 (2008) 214107.
[35] S.D. Brorson, A. Kazeroonian, J.S. Moodera, D.W. Face, T.K. Cheng, E.P. Ippen, M.S. Dresselhaus, G. Dresselhaus, Phys. Rev. Lett. 64 (1990) 2172–2175.
[36] T.Q. Qiu, C.L. Tien, Int. J. Heat Mass Transfer 37 (1994) 2789–2797.
[37] E. Leveugle, D.S. Ivanov, L.V. Zhigilei, Appl. Phys. A: Mater. Sci. Process 79 (2004) 1643–1655.
[38] Z. Lin, R.A. Johnson, L.V. Zhigilei, Phys. Rev. B 77 (2008) 214108.
[39] L.V. Zhigilei, Z. Lin, D.S. Ivanov, in: Proceedings of the 2006 ASME International Mechanical Engineering Congress and Exposition (IMECE2006), 2006 (ASME paper IMECE2006-16305).
[40] L.V. Zhigilei, D.S. Ivanov, E. Leveugle, B. Sadigh, E.M. Bringa, High-power Laser Ablation V, Proc. SPIE, vol. 5448, 2004, 505–519.
[41] D.S. Ivanov, L.V. Zhigilei, Phys. Rev. Lett. 91 (2003) 105701.